1 **Evaluation of the optimal activation parameters for almond shell bio-char production**

2 **for capacitive deionization**

3 Maniscalco M. P.[1,3], Corrado C.[2],Volpe R.[3] and Messineo A.[1]*

4 *[1]Faculty of Engineering and Architecture, Kore University of Enna, Cittadella Universitaria,*

5 *94100 Enna, Italy*

6 *[2]Department of BioMedicine, Neurosciences and Advanced Diagnostics (Bi.N.D), Via Divisi*

7 *83, 90133 Palermo, Italy*

8 *[3]School of Engineering and Materials Science, Queen Mary University, London, United*

9 *Kingdom*

10

11 **Abstract**

12 A study on a possible new biomass waste to be used as electrode material for capacitive

13 deionization (CDI) processes was performed. Raw almond shells were pyrolyzed at 800, 900

14 and 1,000 °C and then activated through CO_2. Carbon activation is used to develop porosity

15 inside the material, increasing the specific surface area and the adsorption performances. In

16 this work, authors tried to correlate the effects of pyrolysis and activation temperature on the

17 ion storage capacity. Results from the desalination tests indicated that the best performance in

18 terms of ion adsorption was obtained when the bio-char was activated at the temperature of

19 900 °C. Brunauer-Emmet-Teller (BET) and Barret-Joyner-Halenda (BHJ) analysis confirmed

20 the trend of the CDI tests, reporting the highest surface area and share of micropore sites for

21 the 900 °C samples. Salt adsorption capacity was found to be in the range of 13.7 to 19.2 mg

22 g^{-1}.

23

24 **Keywords**

25 Biomass; Almond shell; Carbon activation; Capacitive deionization.

26

27 **1. Introduction**

28 Fresh water supply is one of the most discussed issues of the last decades (Chen et al., 2011;

29 Z. Chen et al., 2018). On daily basis, almost 100 millions of cubic meters of sea and brackish

30 water need to be desalinated to match the demand for municipal and industrial purposes (Zarzo

*Corresponding author. Tel: +39 0935 536448;

E-mail address: antonio.messineo@unikore.it (A. Messineo).

31   and Prats, 2018). Most of the desalination plants relies on the reverse osmosis technology,

32   followed by the thermal distillation processes (AlMarzooqi et al., 2014). One of the main

33   drawbacks of these system is the environmental pollution due to the energy production to

34   satisfy the plant demand. In fact, as referred by the Global Clean Water Desalination Alliance

35   (GCWDA), approximately 76 million tons of CO_2 are yearly generated worldwide, to produce

36   fresh water from salty sources. It results, therefore, imperative the need of reduce the energy

37   consumption during desalination, in order to mitigate its relative environmental impact. For

38   these reasons, there is an increased attention toward the research of a more eco-friendly

39   approach. Capacitive deionization (CDI) is gaining increased attention due to the potential

40   lower energy consumption when treating brackish water and to the possibility of using waste

41   biomass as precursor for the realization of activated carbons (Chérif et al., 2015; Huyskens et

42   al., 2013; Porada et al., 2013). The analysis conducted by Anderson and his research team

43   (Anderson et al., 2010) showed promising perspective for brackish water desalination through

44   capacitive deionization. To evaluate the process efficiency, authors applied the concept of cycle

45   efficiency used for supercapacitors to the capacitive deionization process, calculating it as the

46   ratio between the recovered energy during discharge and the one spent in charging. The

47   minimum thermodynamic energy needed to remove salt ions from water is known to be

48   approximately 1.1 kWh m^{-3} and 0.12 kWh m^{-3} respectively for sea and brackish water.

49   According to the thermodynamic model proposed by Anderson (Anderson et al., 2010) if CDI

50   can achieve a cycle efficiency of 60-70%, it could become an energetically competitive

51   technology for brackish water desalination. Tests conducted by Welgemoed and Shutte

52   (Welgemoed and Schutte, 2005), reported a round efficiency of approximately 50%, but further

53   improvements could be achieved by increasing the efficiency of the energy recovery process..

54   CDI relies on porous material, like activated carbons, carbon nanotubes or carbon fibers, that

55   electrostatically trap and store salt ions from a brackish water flow, thanks to a voltage

56   difference applied between two electrodes. By inverting the voltage or short-circuiting the

57   system, electrodes can be regenerated, discharging the ions in a bulk solution (Li et al., 2016;

58   Oren, 2008). To be effective in ion sequestration, electrode material must guarantee specific

59   intrinsic properties. In fact, an high surface area, a proper pore distribution, a good electrical

60   conductivity and a good permeability must be guaranteed (Dehkhoda et al., 2016a, 2016b).

61   Both biomass recovered material and artificial porous media, was tested in the last years by

62   numerous research groups (Belaustegui et al., 2018; El-Deen et al., 2014; Zhang et al., 2007).

63   If artificial material on one hand allows to develop a proper structure that boost ion adsorption,

64   one the other hand the very delicate and expensive process to realize them limit the diffusion

65   (Anderson et al., 2010; Oren, 2008). Waste biomass sources can significantly reduce the cost

66   of the activated carbon production, but a lower adsorption capacity must be expected. Different

67   kind of biomasses (P.-A. Chen et al., 2018; Feng et al., 2018; Hou et al., 2015; Lado et al.,

68   2017; Li et al., 2016), as well as carbon nanotubes had been tested during the last years. Waste

69   biomass activated carbons are more and more investigated due to the low prices and the great

70   abundance of the starting materials. Among the best results of the tested biomasses, Feng and

71   his research group (Feng et al., 2018) realized and tested activated carbons made from *Loofa*

72   *sponge* achieving a salt adsorption capacity of 22.5 mg g^{-1}, with an applied voltage between

73   the electrodes of 1V. Similarly, Li and his co-workers (Li et al., 2016) tested the activated

74   carbon produced from cotton waste in a capacitive deionization cell with an applied voltage of

75   1.2 V, resulting in an adsorption capacity of 16.1 mg g^{-1}. Lower salt removal capacity (5 mg g^{-1}

76   ) was reported by Lado et al. (Lado et al., 2017) when using activated carbon made from sugar

77   cane fly ashes, with an applied voltage of 1.2 V. Moreover, the synthesis of artificial porous

78   media starting from polymeric structures, is a very delicate and expensive process compared

79   to the one involving residual.

80   In the present paper, different pyrolysis and activation temperatures were tested for the

81   production of activated carbons from almond shells, in order to study the evolution of the

82   material structure and adsorption capacity. For what is the authors' knowledge no previous

83   tests were conducted on the use of almond shells as precursors material for the electrode

84   fabrication in CDI applications. The aim of the work is to gain information on how this kind

85   of biomass behave and how the activation temperature affect the carbon structure and its

86   adsorption capacity. Physical activation was preferred over chemical one since it can guarantee

87   a good surface area and pore size distribution, without the drawback of dealing with chemical

88   waste. The analysis conducted on the saturated electrodes allowed also to evaluate the

89   adsorption capacity in relation to the internal carbon structure, opening to a new field of

90   possible research on carbon structure for CDI.

91

92   **2. Materials and methods**

93

94   *2.1 Preparation of the activated carbons*

95   Fresh almond shells were collected already dry and stored for further use. Once needed, the

96   almond shells were grinded through a miller (Retsch ZM 200; Germany) and sieved (Retsch

97   AS 200; Germany) in order to obtain particles size lower than 125 μm, dried again in oven at

98   90 °C for 60 h and then stored at the temperature of -20 °C in Argon atmosphere. For the

99   production of the activated carbon, a Carbolite tubular furnace (Carbolite Gero 3216CC

100   Controller; UK) with Ar, N_2 and CO_2 gas feed was used. The biomass was displaced in a

101   ceramic crucible of approximately 30 cm^2, with thickness of the bed of 1.5-2 mm. The crucible

102   was then placed in the centre of the furnace and Ar was fluxed at 2 L min^{-1} for 10 min to ensure

103   an inert environment inside the reactor, before starting the pyrolysis. Biomass was then

104   carbonized at 800, 900 and 1000 °C at a heating rate of 10 °C min^{-1} under an Argon flow of

105   1.2 L min^{-1}. Once the peak temperatures were reached, chars were firstly carbonized for 10 min

106   in Argon and then activated by switching to CO_2 for 15 min, keeping the same flow rate as

107   before. Once the process was finished, the furnace was let to cool down to ambient temperature

108   in Argon atmosphere and activated carbons were weighted and stored. The samples obtained

109   were named AC800, AC900 and AC1000 respectively for the ones produced at 800, 900 and

110   1000 °C.

111

112   *2.2 Preparation of the electrodes*

113   Activated carbons were used to prepare the carbon electrodes for the CDI experiments. ACs

114   were initially mixed with polyvinylidene fluoride (PVDF-Sigma Aldrich 24937-79-9;

115   Missouri, USA) in a ratio of 9:1 (w/w) for 5 minutes using mortar and pestle. Once an

116   homogeneous matrix was obtained, N-Methyl-2-pyrrolidone (NMP-Sigma Aldrich 872-50-4;

117   Missouri, USA) was added and mixed for further 20 minutes to dissolve the binder and obtain

118   a slurry of the desired consistence. To produce the electrodes, the carbon paste was coated on

119   a current collector (MTI Corporation – EQ-CC-Al-18u-260; California, USA) using a wire bar

120   (K-hand coater) and then shaped to the desired dimensions (42 mm X 27mm). Electrode

121   thickness was calculated to be approximately 130 μm. The carbon paste was dried in oven at

122   80 °C for 72 h and then weighted and stored. The mass of each electrode was calculated by

123   weight difference between the dried electrode and the current collector and was equal to 0.06

124   g.

125

126   *2.3 Material characterization*

127   Morphology and structure of the activated carbon produced were studied with the Scanning

128   Electron Microscope (SEM FEI Inspect-F; Oregon, USA) and the Transmission Electron

129   Microscope (TEM JEOL 2010; Japan), while for the chemical composition the study of Energy

130   Dispersive Spectroscopy (EDS) spectra was performed. Specific surface area and pore size

131   distribution were evaluated through Brunauer-Emmet-Teller (BET) and Barret-Joyner-

132   Halenda (BJH) analysis with Nova 4200e (Austria). SEM was also used to investigate the

changes in the surface structure between the activated carbons and the produced electrodes, to check whether the use of the binder caused changes in the morphology of the samples. For this purpose, saturated electrodes were dried in oven at 95 °C to 72 h and then crushed again to obtain a carbon powder.

2.4 Electrodes testing

Electrodes were tested in a CDI cell. For each type of activated carbons, two different electrodes pairs were made and tested. Before starting the adsorption test, the cell was assembled and deionized water was fluxed for 2 h to remove any detachable particles from the electrode surface that could otherwise influence the following measurements. For the desalination tests, it was continuously recirculated a 50 ml of a 500 mg L^{-1} NaCl (>99%, Sigma-Aldrich; Missouri, USA) solution at a flow rate of 10 ml min^{-1} from the main becker to the cell, by means of a peristaltic pump (Watson Marlow 323; UK). Between the two electrodes it was applied a voltage difference of 1.2V, ensured by a power supply (EA 3048b; Germany), and the salt concentration was continuously measured inside the becker by means of a conductivity meter (Reed SD-4307 Conductivity/TDS/Salinity Datalogger; USA). Adsorption tests lasted 120 min and the salt adsorption capacity (SAC) of each electrodes pair was evaluated through equation 1:

$$SAC = \frac{(C_{in} - C_{fin}) * V}{m_{el}} \quad [\text{mg g}^{-1}] \hspace{4cm} \text{Eq. 1}$$

Where:

C_{in} is the initial salt concentration in mg L^{-1};

C_{fin} is the final salt concentration in mg L^{-1};

V is the solution volume in L;

m_{el} is the total electrode mass in g.

3. Results and discussion

3.1 Morphology and structure of the activated carbons

Pyrolysis and activation led to a mass loss in the samples due to the removal of most of the volatile compounds (Volpe et al., 2017). The mass yields of the produced activated carbon were calculated once the carbons had cooled down to room temperature, and were found equal to 27%, 24% and 24% respectively for AC800, AC900 and AC1000. The morphological

165   analysis conducted with the SEM showed the presence and the formation of pores on the
166   external surface of the material as well as bubbling phenomena, possibly due to deposition or
167   melting (Volpe et al., 2015). The bubbling phenomena increase the pores dimension of the
168   material, improving the mass transport. As long as pyrolysis proceed, the generated volatile
169   matter remain confined inside the particle, forming bubbles (Yu et al., 2007). The larger the
170   particle, the harder is for the activating agent to diffuse inside and develop porosity, as well as
171   for the produced gases to escape from the particle core. Once the bubble reach the surface, it
172   explode releasing the volatiles. The whole process is known to further increase the porosity of
173   the material (Valdés et al., 2018).

174   On the external surface, there were found pores with diameter in the range of 10-35μm which
175   can act as main pathways to reach the micro and nanopores in the inner part of the activated
176   carbon, as also referred in (Fukuyama et al., 2001; Martínez et al., 2006; Zabaniotou et al.,
177   2008). In Fig 1 a-e it can be seen the pores development on the outer surface of the samples
178   (Fig 1 c) as well as an increase in the pore diameter of the already existing holes and a reduction
179   of the thickness of the external wall of the particles, possibly due to the shrinking phenomena
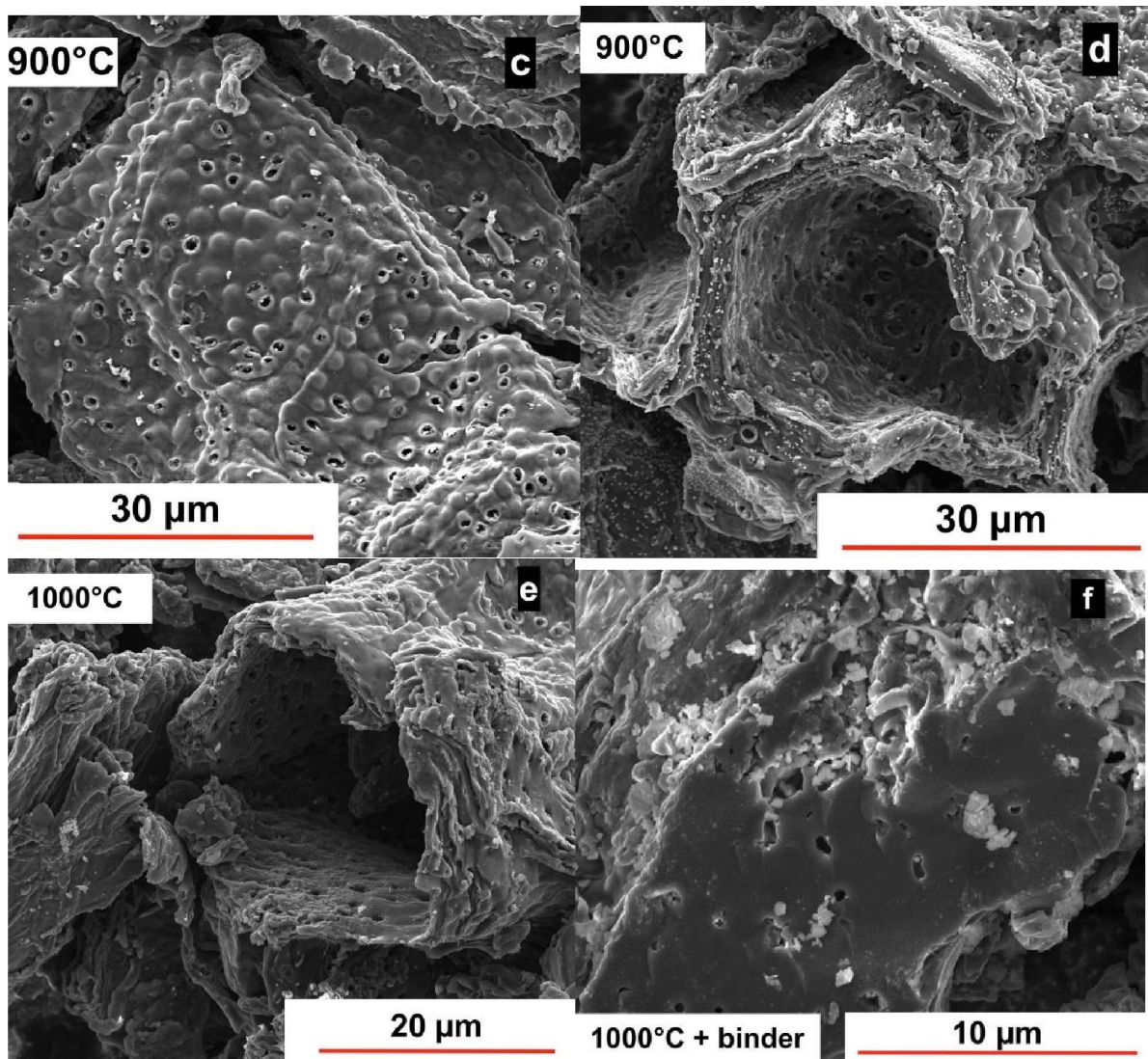180   and the removal of volatile compounds.
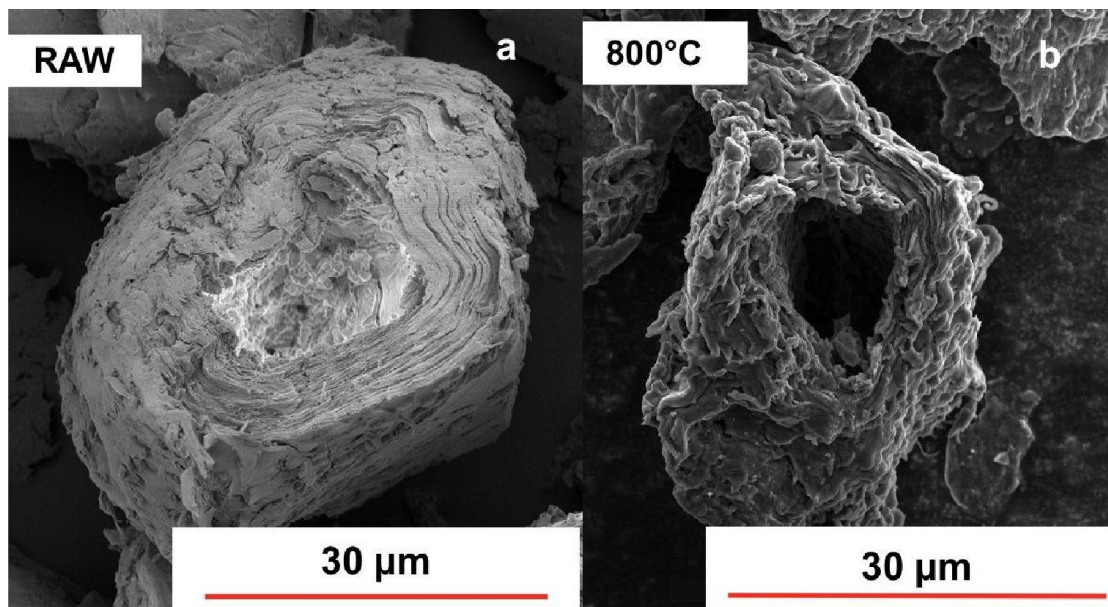
181

Fig. 1 SEM images of: a) raw almond shells; b) AC800; c) AC900; d) AC900; e) AC1000; f) AC1000+binder.

The already existing holes in the raw material present diameter in the range of 15-17 μm, while in the activated carbons it is increased up to 30-35 μm. The role of CO_2 in carbon activation and pore structure development was already investigated by Rodriguez-Reinoso and his co-worker for the production of activated carbon from peach stones (Rodriguez-Reinoso et al., 1992). Authors found that the action of CO_2 is more evident as long as the activation temperature increase, when performing pyrolysis and activation at temperatures within 850 °C. As also reported by Kennedy and his co-workers (Kennedy et al., 2005), during pyrolysis most of the volatile compounds are released from the biomass, creating new holes in the structure while part of the cellulose and lignin are converted into carbon. However, some of the volatiles produced during pyrolysis might re-polymerize and condensate on the external surface of the chars clogging part of the existing pores. The following physical activation stage is needed to remove the tar deposit as well as reopening the blocked pores and create new ones (Pallarés et

197　al., 2018). The reducing atmosphere, due to the presence of CO_2, mostly for temperatures above

198　700 °C, lead to a partial gasification according to the reverse of the Boudouard reaction (eq.

199　2), increasing the adsorption capacity of the material.

200　$C + CO_2 \rightarrow 2CO$　　　　　　　　　　　　　　　　　　　　　　　　　　　　　eq. 2

201　The investigation conducted on the surface of the activated carbon mixed with binder (Fig. 1f),

202　showed a partial pore occlusion due to binder deposition on the outer carbon surfaces. To gain

203　information on the surface composition, it was performed an EDS analysis on the AC1000

204　electrode, to get an overview of the chars composition. The surveys on the external surface

205　reveal a sample composition made of 83.4 % of carbon, 11.1% of oxygen, 3.1 % of fluorine,

206　1.7 % of sodium and 0.6 % of aluminium, based on weight. The presence of fluorine is strictly

207　due to the use of the binder. Moreover, it was also observed a significant evolution in the

208　internal structure of the three different carbons. The formation of graphitic layers can clearly

209　be seen in AC800 (white circular spots in Fig 2a,b) together with a broader area of amorphous

210　carbon. Graphite layers present spacing in the range of 0.13-0.33 nm, which could be due to

211　different orientation of the crystals. In fact, the measure of 0.13 nm could be relative to the

212　distance in the carbon covalent bonds while, being the reported distance for graphite planes

213　equal to 0.34 nm, the measurement of 0.33 nm could be a good approximation of this case. Fig

214　2c reveals a more uniform internal structure for AC900 with respect to the other two samples.

215　No evidences of graphitic layers were found even if, since they were spotted in the other

216　carbons, there should be present in the material.

217　AC1000 (Fig 2d) presents onion rings structure characteristic of the carbon cluster formation

218　(Hoekstra et al., 2015) with outer diameters of the rings in the range of 15-25 nm, and an

219　internal diameter of approximately 9 nm. The number of layers was between 11 and 14, within

220　all the onions-shaped formations,. The increase in pyrolysis temperature induced significant

221　changes in the internal structure of the material, increasing the degree of graphitization. Similar

222　considerations were proposed by Guizani and his research group (Guizani et al., 2017), which

223　found that for pyrolysis temperature above 600 °C, graphene-like structures were generated

224　due the crystallization of the polyaromatic compounds released during the process.

225　These particular constitutions, increasing in size, lead toward a transformation of the

226　amorphous phase to more ordered graphitic-like structure (Debiagi et al., 2018). Also Billaud

227　et al. (Billaud et al., 2016) found an increase in soot formation from 800°C with a steep increase

228　for temperature above 1000 °C.

229 The formation of soot particles for temperatures above 1000 °C was confirmed by Quin and
230 his research group (Qin et al., 2012), as well as by Wang et al (Wang et al., 2018). In (Wang
231 et al., 2018) authors refer of a linear increase in soot yield, on weight, from 0.47% to 5.95%
232 when the pyrolysis temperature of wheat straw was raised from 1000 °C to 1200 °C, while no
233 trace was found in the sample pyrolyzed at 900 °C. The process of soot formation is still under
234 discussion among the scientific community. One of the of possible the pathways of sooth
235 growth on which many researchers agree on is the nucleation starting from polycyclic aromatic
236 hydrocarbons (PAH), even though the process in detail is not yet fully understood (D'Anna,
237 2009; Debiagi et al., 2016; Frenklach and Mebel, 2020; Wang and Chung, 2019). During
238 biomass pyrolysis the released PAH from the decomposition of lignin, bonding and growing
239 in size lead to the nucleation of soot particles. A detailed discussion of soot formation was
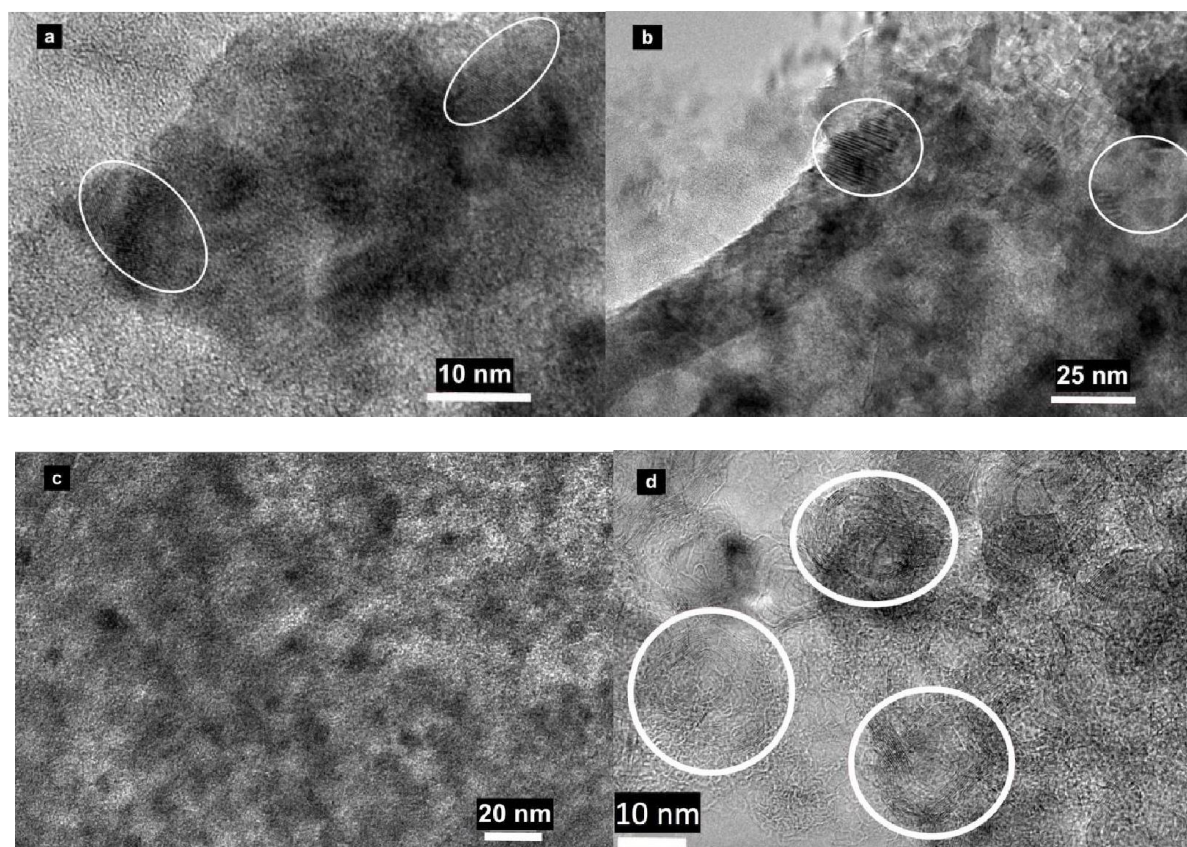240 proposed by Franklach and Mabel in (Frenklach and Mebel, 2020).

241

242
243
Fig. 2 TEM images of a,b) AC800, c) AC900 and d) AC1000.

244 *3.2 Surface area and pore size distribution analysis*
245 The analysis of the specific surface area and the pore size distribution of the three samples
246 revealed an increase in the porosity when raising the activation temperature from 800 °C to
247 900 °C. In Fig. 3 and Fig. 4 are reported the curves of the adsorbed gas volume and the
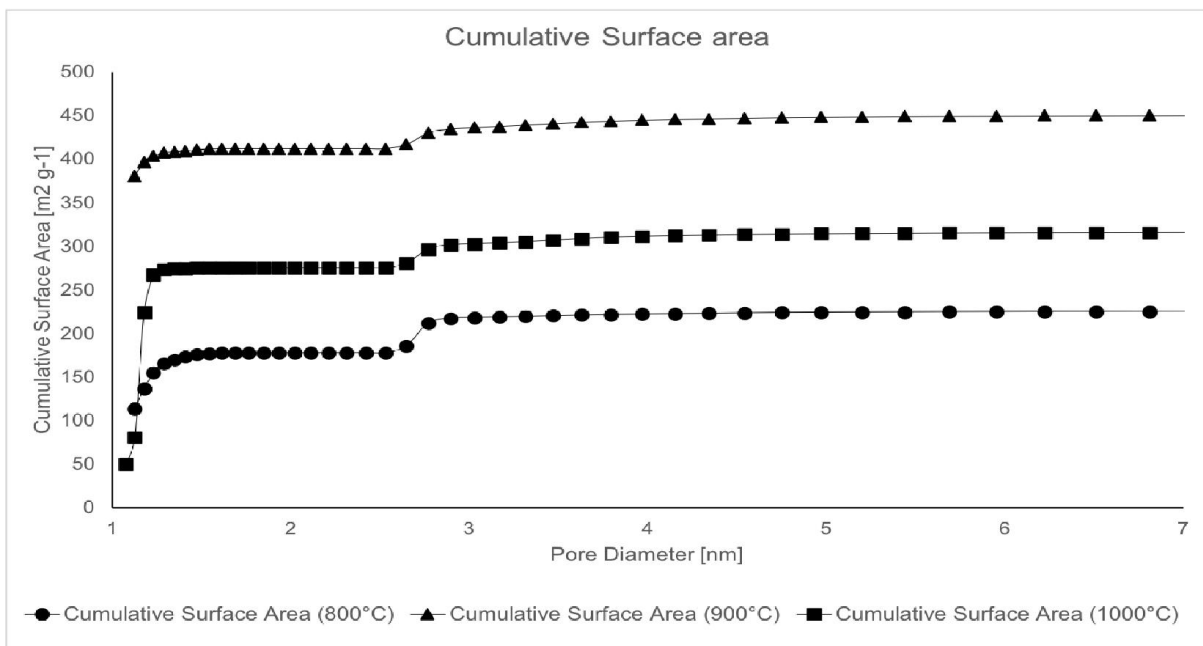
248   cumulative surface area for AC800, AC900 and AC1000. When the activation temperature is

249   increased from 800 °C to 900 °C, the specific surface area is almost doubled, raising from

250   226.3 m^2 g^{-1} to 452.2 m^2 g^{-1}.
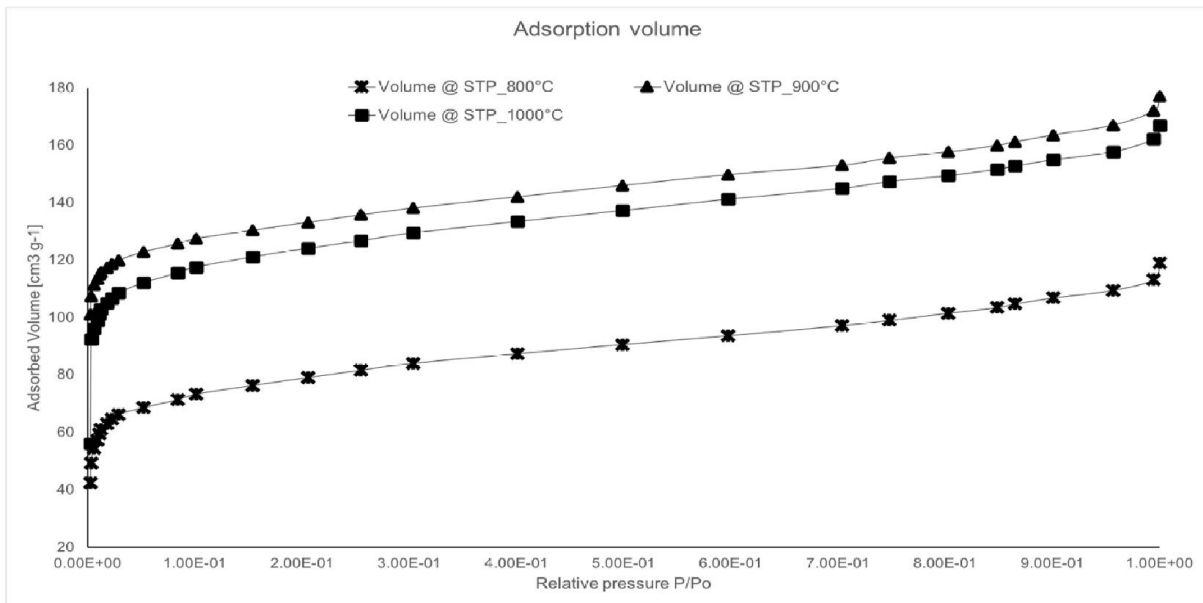
251

252   Fig. 3 Adsorption volume for AC800, AC900 and AC1000.

253   A further increase in the activation temperature up to 1000 °C led to a reduction in the specific

254   area of almost 30%, reaching 317.4 m^2 g^{-1}. All the three curves present the classic behaviour

255   of the Type 1 isotherm, according to the IUPAC classification, with an steep increase in the

256   absorbed volume for relative pressure < 0.2 P/P$_0$, followed by steady increment until P/P$_0$ =

257   0.9.

258

259   Fig. 4 Cumulative Surface Area for AC800, AC900 and AC1000.

260 The initial part of the adsorption curve represents the contribution of micro-porosity to the total

261 surface area, which it can clearly be see that result predominant in all of the three activated

262 carbon samples. the second branch of the curve is characterized by an almost flat trend,

263 indicating the lack of larger pores in the material.

264 In terms of volume of gas adsorbed, the difference between AC900 and AC1000 is lower than

265 for the cumulative surface area, presenting a 5.5% decrease from 177 to 167 cm^3 g^{-1}, while for

266 AC800 was 118 cm^3 g^{-1}. The study of the pore size distribution reveals also a significative

267 change in the pore development inside the activated carbons (Fig.5).
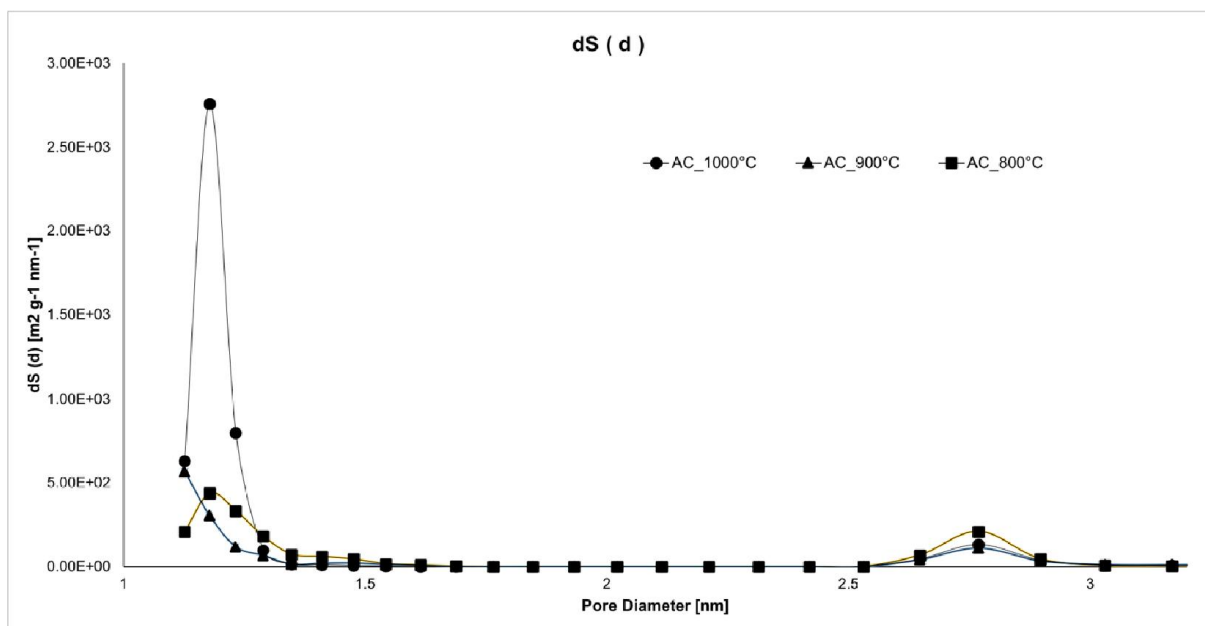
268

269 Fig. 5 Pore size distribution for AC800, AC900 and AC1000.

270 Comparing the results reported in Fig. 5 with the ones in Fig. 4, it can be noticed that the share

271 of micropores with diameter <1 nm change significantly when varying the activation

272 temperature. Indeed, while for AC1000 only 16 % of the pores present diameters <1 nm, for

273 AC800 is 50 % while for AC900 it raises up to 84 %. These results could indicate a variation

274 in the carbon structure when changing the activation temperature. In fact, the analysis reported

275 showed a non-linear correlation between the increase in the activation temperature and the

276 increase in surface area and micropore development. This could be due to the higher degree of

277 carbonization, as also confirmed by the TEM images, which could imply a re-organization of

278 the internal structure as well as a widening of the already existing pores.

279 Similar results were also reported in (Dehkhoda et al., 2014) for carbon activation in the

280 temperature range of 675-1,000 °C due to micropore collapse when reaching the highest

281 temperature and the formation of a more ordered structure. Micropore enlargement at high

282 temperature due to pore walls collapse was also reported by Zhang and his co-workers (Zhang

11

283 et al., 2004) when activating agricultural residues through CO_2. Authors also reported an
284 increase in the severity of the phenomena as long as the activation time increase. Increase in
285 surface area for temperature range of 500-900 °C were also reported by Lua and Gou when
286 testing activation of oil palm shell (Lua and Guo, 2001). Authors found a raise in surface area
287 for the 900 °C sample when the activation time was kept within 30 min, while a significant
288 decrease was encountered when char was maintained under CO_2 for 60 min. This result,
289 according to the authors, was related to a strong interaction in the CO_2-carbon reaction.

290

291 *3.3 Salt adsorption capacity*

292 Electrode testing was conducted with an initial salt concentration of 500 mg L^{-1} and an applied
293 voltage of 1.2 V. Each adsorption test was run in duplicate and the average of the two different
294 runs was also reported in the graphs of Fig. 6. For all the three samples, the saturation of the
295 electrodes was reached after 120 minutes from the beginning of the tests. AC900 showed the
296 best salt adsorption capacity, with up to 19.2 mg of adsorbed salt for each gram of electrode
297 material, while AC800 and AC1000 reached 14.6 and 13.7 mg g^{-1}, respectively. The obtained
298 results are in line with the micro-porosity development of the three different samples. Indeed,
299 it is well established that ion storage is mostly performed inside the pores with diameter lower
300 than 1 nm (Dykstra et al., 2016; Li et al., 2017; Zhang et al., 2019). In fact, despite the higher
301 surface area of AC1000 with respect to AC800, the lower amount of micropore sites could
302 determine an inferior adsorption capacity. At the same time, the highest surface area and
303 micropore sites of the AC900 determined a significantly better performance when tested inside
304 the CDI cell. In fact, despite the higher surface area of AC1000 with respect to AC800, the
305 lower amount of micropore sites could determine an inferior adsorption capacity. At the same
306 time, the highest surface area and micropore sites of the AC900 determined a significantly
307 better performance when tested inside the CDI cell.

308 Similar trend regarding specific surface area and adsorption capacity for biomass samples
309 treated at 800, 900 and 1000 °C was found in (Liu et al., 2019) by Liu and his co-workers when
310 testing pine pollen char for capacitive deionization. Authors reported a significant decrease (-
311 38%) in specific surface area when the temperature was raised from 900 °C to 1000 °C,
312 together with a lower ion adsorption. Results from the CDI experiment showed the lowest
313 potential for NaCl removal for the carbon realized at 1000 °C while the best result was obtained
314 for the 900 °C treatment.

315

316
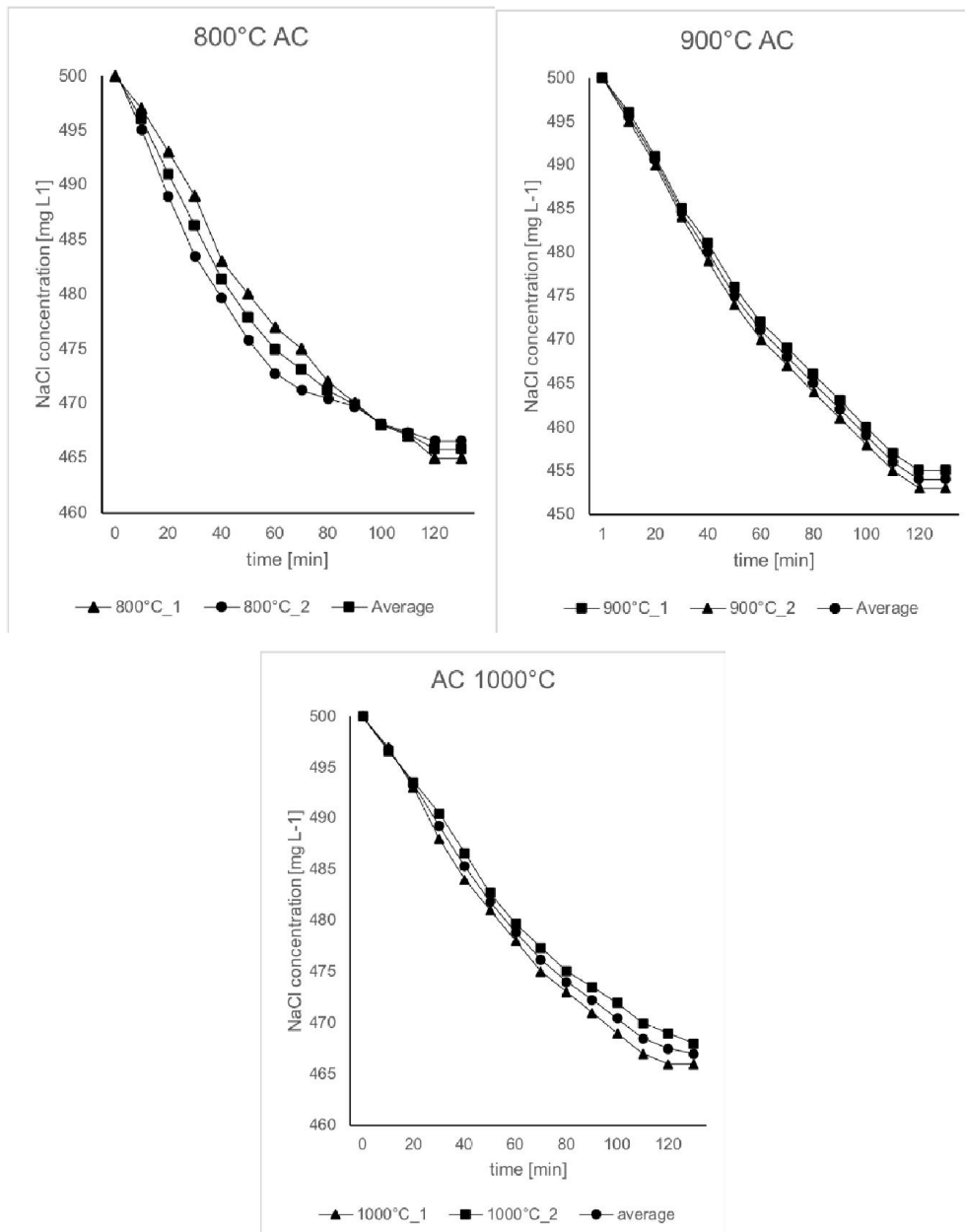
317

318

Fig. 6 Results of desalination tests: adsorption capacity.

319 The adsorption kinetics was studied through the pseudo-first order (eq. 3) (Simonin, 2016) and

320 a pseudo-second (eq. 4) (Robati, 2013) order model, which can be formulated as:

321 $$ln\left[\frac{q_e-q_t}{q_e}\right] = -kt \qquad \text{eq. 3}$$

322 $$\frac{t}{q_t} = \frac{t}{q_e} + \frac{1}{K_2 * q_e^2} \qquad \text{eq. 4}$$

323 Where q_e and q_t are the amount of NaCl adsorbed (in mg g^{-1}) at time t and equilibrium, k and

324 k_2 are respectively the first and second order constant of adsorption, and t is the time. Between

325 the two models, it was selected the one that presents the higher correlation coefficient R^2. The

326 values of R^2 for the pseudo-first order and pseudo-second order models and for all the three

327 activated carbons are resumed in Tab. 1. It can clearly be seen that the second order kinetic

presents a weak correlation for all of the activated carbons, while the first-order fit very well with the data collected from the experiments. Equation 2 was plotted for the three activated carbons and results are reported in Fig. 7.

Sample	R^2	
	1st order	2nd order
AC800	0.97	0.57
AC900	0.91	0.67
AC1000	0.91	0.84

Table 1. Pseudo-first and pseudo-second order kinetic correlation coefficient.
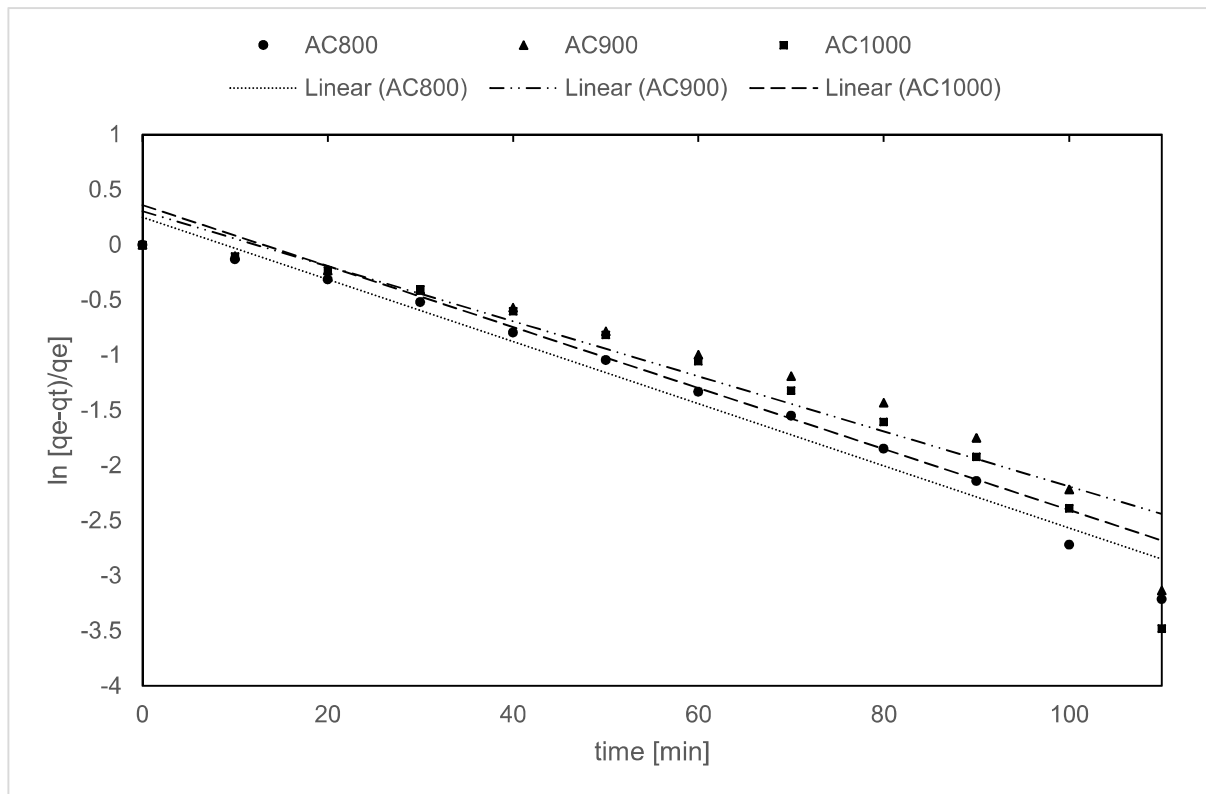
Fig. 7. Pseudo-first order kinetics.

The saturated electrodes were further studied through SEM/EDS and TEM/EDS analysis. For the Na^+ saturated electrode, when evaluating the external composition through a SEM/EDS analysis, there was found an increase in the sodium concentration when inspecting the main outer pores of the material with sodium concentration raising up to 4.03 % (w/w) from the starting value of 1.76 % obtained during the surveys on AC1000.

344   *3.4 Perspective, applications and future works*

345   Even if numerous researches has been conducted over the last years on CDI, the present

346   technology is still far away from a possible industrial scale application. The main aspects on

347   which the scientific community is working on are the development of a proper carbon internal

348   structure, the reduction of losses inside the cell and the energy recovery from the electrode

349   regeneration step. An appropriate electrode hierarchical porosity can enhance the velocity and

350   the electrosorption capacity, promoting the fluid diffusion inside the material and the ion

351   storage in the micropore sites. Regarding the energy recovery processes, two pioneering works

352   was proposed by García-Quismondo and his research group (García-Quismondo et al., 2013)

353   and by Dlugołęcki et al., (Długołecki and Van Der Wal, 2013). In this latter work, thanks to

354   the optimization of the electrode regeneration step, authors were able to reduce the energy

355   consumption up to 0.26 kWh m^{-3} for a brackish water desalination system, making it

356   competitive with the traditional processes.

357   Aside from the traditional application in deionization systems, the possibility of coupling CDI

358   with renewable energy sources and the easily scalable dimension of the plant, makes this

359   technology suitable even for the installation in remote locations or developing countries

360   (Mossad et al., 2013). Different studies was conducted to verify such hypothesis running small

361   plants, even in an off-grid condition. These consideration could make CDI an optimal solution

362   for isolated villages who have only access to brackish water sources and no direct connection

363   to the electric grid. Tang and his research group (Tan et al., 2018) studied the possible

364   connection of a 5 m^3 day^{-1} membrane capacitive deionization plant to a photovoltaic plant to

365   furnish the energy needed. Another technical solution based on renewable energy sources, has

366   been proposed by Forrestal et al., (Forrestal et al., 2012) who studied the possible use of a CDI

367   system fuelled by a microbial cell. Authors were able to satisfy the energy need, obtaining also

368   significant results in terms of total dissolved solid removal.

369   It could also be useful to broader the present research to analyse more in depth the transition

370   from the activation temperature of 900°C to 1000°C, since within this range seems to happen

371   the more evident modifications inside the char particles. At the same time, evaluating how the

372   activation time affect the final material could drive to a proper procedure to obtain the best

373   adsorption capacity from the starting biomass sample.

374   A further study is in progress at the moment, trying to couple crystallography analysis, with

375   ion adsorption capacity. In order to be effective, authors are trying to find various

376   monocrystalline, polycrystalline and amorphous carbon sites to evaluate their Sodium and

377 Chlorine concentrations, in order to define possible adsorption trends in relation to the carbon
378 structure.

4. Conclusion

380 The evolution of the structure and the adsorption behaviour of three different activated carbon
381 were investigated. Significant changes in the specific surface area and pore size distribution
382 were found when raising the activation temperature from 800 to 1000 °C. Cumulative surface
383 area was found equal to 225, 450 and 316 $m^2 g^{-1}$ respectively for AC800, AC900 and AC1000.
384 Nevertheless, the adsorption capacity did not follow the same trend, presenting a reduction of
385 28 %, form 19.2 to 13.7 mg g^{-1}, when the activation temperature was increased from 900 to
386 1000 °C.

387

392

References

394 Al Marzooqi, F.A., Al Ghaferi, A.A., Saadat, I., Hilal, N., 2014. Application of Capacitive
395 Deionisation in water desalination: A review. Desalination.
396 https://doi.org/10.1016/j.desal.2014.02.031

397 Anderson, M.A., Cudero, A.L., Palma, J., 2010. Capacitive deionization as an electrochemical
398 means of saving energy and delivering clean water. Comparison to present desalination
399 practices: Will it compete? Electrochim. Acta 55, 3845–3856.
400 https://doi.org/10.1016/J.ELECTACTA.2010.02.012.

401 Belaustegui, Y., Zorita, S., Fernández-Carretero, F., García-Luis, A., Pantò, F., Stelitano, S.,
402 Frontera, P., Antonucci, P., Santangelo, S., 2018. Electro-spun graphene-enriched carbon
403 fibres with high nitrogen-contents for electrochemical water desalination. Desalination
404 428, 40–49. https://doi.org/10.1016/J.DESAL.2017.11.019.

405 Billaud, J., Valin, S., Peyrot, M., Salvador, S., 2016. Influence of H2O, CO2 and O2 addition
406 on biomass gasification in entrained flow reactor conditions: Experiments and modelling.
407 Fuel 166, 166–178. https://doi.org/10.1016/J.FUEL.2015.10.046.

408 Chen, P.-A., Cheng, H.-C., Wang, H.P., 2018. Activated carbon recycled from bitter-tea and
409   palm shell wastes for capacitive desalination of salt water. J. Clean. Prod. 174, 927–932.
410   https://doi.org/10.1016/J.JCLEPRO.2017.11.034.

411 Chen, Z., Song, C., Sun, X., Guo, H., Zhu, G., 2011. Kinetic and isotherm studies on the
412   electrosorption of NaCl from aqueous solutions by activated carbon electrodes.
413   Desalination 267, 239–243. https://doi.org/10.1016/J.DESAL.2010.09.033.

414 Chen, Z., Zhang, H., Wu, C., Luo, L., Wang, C., Huang, S., Xu, H., 2018. A study of the effect
415   of carbon characteristics on capacitive deionization (CDI) performance. Desalination 433,
416   68–74. https://doi.org/10.1016/J.DESAL.2017.11.036.

417 Chérif, M., Mkacher, I., Dammak, L., Ben Salah, A., Walha, K., Grande, D., Nikonenko, V.,
418   2015. Water desalination by neutralization dialysis with ion-exchange membranes: Flow
419   rate and acid/alkali concentration effects. Desalination 361, 13–24.
420   https://doi.org/10.1016/J.DESAL.2015.01.024.

421 D'Anna, A., 2009. Combustion-formed nanoparticles. Proc. Combust. Inst.
422   https://doi.org/10.1016/j.proci.2008.09.005.

423 Debiagi, P.E.A., Gentile, G., Cuoci, A., Frassoldati, A., Ranzi, E., Faravelli, T., 2018. Yield,
424   Composition and Active Surface Area of Char from Biomass Pyrolysis. Chem. Eng.
425   Trans. 65, 97-102 SE-Research Articles. https://doi.org/10.3303/CET1865017.

426 Debiagi, P.E.A., Gentile, G., Pelucchi, M., Frassoldati, A., Cuoci, A., Faravelli, T., Ranzi, E.,
427   2016. Detailed kinetic mechanism of gas-phase reactions of volatiles released from
428   biomass pyrolysis. Biomass and Bioenergy.
429   https://doi.org/10.1016/j.biombioe.2016.06.015.

430 Dehkhoda, A.M., Ellis, N., Gyenge, E., 2016a. Effect of activated biochar porous structure on
431   the capacitive deionization of NaCl and ZnCl2 solutions. Microporous Mesoporous
432   Mater. 224, 217–228. https://doi.org/10.1016/J.MICROMESO.2015.11.041.

433 Dehkhoda, A.M., Ellis, N., Gyenge, E., 2014. Electrosorption on activated biochar: Effect of
434   thermo-chemical activation treatment on the electric double layer capacitance. J. Appl.
435   Electrochem. https://doi.org/10.1007/s10800-013-0616-4.

436 Dehkhoda, A.M., Gyenge, E., Ellis, N., 2016b. A novel method to tailor the porous structure
437   of KOH-activated biochar and its application in capacitive deionization and energy
438   storage. Biomass and Bioenergy 87, 107–121.

439 https://doi.org/10.1016/J.BIOMBIOE.2016.02.023.

440 Długołecki, P., Van Der Wal, A., 2013. Energy recovery in membrane capacitive deionization.
441   Environ. Sci. Technol. https://doi.org/10.1021/es3053202

442 Dykstra, J.E., Zhao, R., Biesheuvel, P.M., van der Wal, A., 2016. Resistance identification and
443   rational process design in Capacitive Deionization. Water Res. 88, 358–370.
444   https://doi.org/10.1016/J.WATRES.2015.10.006.

445 El-Deen, A.G., Barakat, N.A.M., Khalil, K.A., Kim, H.Y., 2014. Hollow carbon nanofibers as
446   an effective electrode for brackish water desalination using the capacitive deionization
447   process. New J. Chem. https://doi.org/10.1039/c3nj00576c.

448 Feng, C., Chen, Y.-A., Yu, C.-P., Hou, C.-H., 2018. Highly porous activated carbon with multi-
449   channeled structure derived from loofa sponge as a capacitive electrode material for the
450   deionization of brackish water. Chemosphere 208, 285–293.
451   https://doi.org/10.1016/J.CHEMOSPHERE.2018.05.174.

452 Forrestal, C., Xu, P., Ren, Z., 2012. Sustainable desalination using a microbial capacitive
453   desalination cell. Energy Environ. Sci. https://doi.org/10.1039/c2ee21121a.

454 Frenklach, M., Mebel, A.M., 2020. On the mechanism of soot nucleation. Phys. Chem. Chem.
455   Phys. 22, 5314–5331. https://doi.org/10.1039/D0CP00116C.

456 Fukuyama, K., Kasahara, Y., Kasahara, N., Oya, A., Nishikawa, K., 2001. Small-angle X-ray
457   scattering study of the pore structure of carbon fibers prepared from a polymer blend of
458   phenolic resin and polystyrene. Carbon N. Y. https://doi.org/10.1016/S0008-
459   6223(00)00159-7.

460 García-Quismondo, E., Santos, C., Lado, J., Palma, J., Anderson, M.A., 2013. Optimizing the
461   energy efficiency of capacitive deionization reactors working under real-world
462   conditions. Environ. Sci. Technol. https://doi.org/10.1021/es4021603.

463 Guizani, C., Haddad, K., Limousy, L., Jeguirim, M., 2017. New insights on the structural
464   evolution of biomass char upon pyrolysis as revealed by the Raman spectroscopy and
465   elemental analysis. Carbon N. Y. 119, 519–521.
466   https://doi.org/10.1016/J.CARBON.2017.04.078.

467 Hoekstra, J., Beale, A.M., Soulimani, F., Versluijs-Helder, M., Geus, J.W., Jenneskens, L.W.,
468   2015. Base metal catalyzed graphitization of cellulose: A combined Raman spectroscopy,
469   temperature-dependent X-ray diffraction and high-resolution transmission electron

470   microscopy study. J. Phys. Chem. C. https://doi.org/10.1021/acs.jpcc.5b00477.

471   Hou, C.-H., Liu, N.-L., Hsi, H.-C., 2015. Highly porous activated carbons from resource-
472   recovered Leucaena leucocephala wood as capacitive deionization electrodes.
473   Chemosphere 141, 71–79. https://doi.org/10.1016/J.CHEMOSPHERE.2015.06.055.

474   Huyskens, C., Helsen, J., de Haan, A.B., 2013. Capacitive deionization for water treatment:
475   Screening of key performance parameters and comparison of performance for different
476   ions. Desalination 328, 8–16. https://doi.org/10.1016/J.DESAL.2013.07.002.

477   Kennedy, L.J., Vijaya, J.J., Sekaran, G., 2005. Electrical conductivity study of porous carbon
478   composite derived from rice husk. Mater. Chem. Phys. 91, 471–476.
479   https://doi.org/10.1016/J.MATCHEMPHYS.2004.12.013.

480   Lado, J.J., Zornitta, R.L., Calvi, F.A., Martins, M., Anderson, M.A., Nogueira, F.G.E.,
481   Ruotolo, L.A.M., 2017. Enhanced capacitive deionization desalination provided by
482   chemical activation of sugar cane bagasse fly ash electrodes. J. Anal. Appl. Pyrolysis 126,
483   143–153. https://doi.org/10.1016/J.JAAP.2017.06.014.

484   Li, G.-X., Hou, P.-X., Zhao, S.-Y., Liu, C., Cheng, H.-M., 2016. A flexible cotton-derived
485   carbon sponge for high-performance capacitive deionization. Carbon N. Y. 101, 1–8.
486   https://doi.org/10.1016/J.CARBON.2015.12.095.

487   Li, Y., Jiang, Y., Wang, T.-J., Zhang, C., Wang, H., 2017. Performance of fluoride
488   electrosorption using micropore-dominant activated carbon as an electrode. Sep. Purif.
489   Technol. 172, 415–421. https://doi.org/10.1016/J.SEPPUR.2016.08.043.

490   Liu, Q., Li, X., Wu, Y., Qing, M., Tan, G., Xiao, D., 2019. Pine pollen derived porous carbon
491   with efficient capacitive deionization performance. Electrochim. Acta 298, 360–371.
492   https://doi.org/10.1016/J.ELECTACTA.2018.12.072.

493   Lua, A.C., Guo, J., 2001. Microporous oil-palm-shell activated carbon prepared by physical
494   activation for gas-phase adsorption. Langmuir. https://doi.org/10.1021/la010290c.

495   Martínez, M.L., Torres, M.M., Guzmán, C.A., Maestri, D.M., 2006. Preparation and
496   characteristics of activated carbon from olive stones and walnut shells. Ind. Crops Prod.
497   23, 23–28. https://doi.org/10.1016/J.INDCROP.2005.03.001.

498   Mossad, M., Zhang, W., Zou, L., 2013. Using capacitive deionisation for inland brackish
499   groundwater desalination in a remote location. Desalination.
500   https://doi.org/10.1016/j.desal.2012.05.021.

501   Oren, Y., 2008. Capacitive deionization (CDI) for desalination and water treatment — past,
502   present and future (a review). Desalination 228, 10–29.
503   https://doi.org/10.1016/J.DESAL.2007.08.005.

504   Pallarés, J., González-Cencerrado, A., Arauzo, I., 2018. Production and characterization of
505   activated carbon from barley straw by physical activation with carbon dioxide and steam.
506   Biomass and Bioenergy. https://doi.org/10.1016/j.biombioe.2018.04.015.

507   Porada, S., Zhao, R., van der Wal, A., Presser, V., Biesheuvel, P.M., 2013. Review on the
508   science and technology of water desalination by capacitive deionization. Prog. Mater. Sci.
509   58, 1388–1442. https://doi.org/10.1016/J.PMATSCI.2013.03.005.

510   Qin, K., Jensen, P.A., Lin, W., Jensen, A.D., 2012. Biomass gasification behavior in an
511   entrained flow reactor: Gas product distribution and soot formation. Energy and Fuels.
512   https://doi.org/10.1021/ef300960x.

513   Robati, D., 2013. Pseudo-second-order kinetic equations for modeling adsorption systems for
514   removal of lead ions using multi-walled carbon nanotube. J. Nanostructure Chem. 3, 55.
515   https://doi.org/10.1186/2193-8865-3-55.

516   Rodriguez-Reinoso, F., Molina-Sabio, M., Muñecas, M.A., 1992. Effect of microporosity and
517   oxygen surface groups of activated carbon in the adsorption of molecules of different
518   polarity. J. Phys. Chem. https://doi.org/10.1021/j100185a056.

519   Simonin, J.P., 2016. On the comparison of pseudo-first order and pseudo-second order rate
520   laws in the modeling of adsorption kinetics. Chem. Eng. J.
521   https://doi.org/10.1016/j.cej.2016.04.079.

522   Tan, C., He, C., Tang, W., Kovalsky, P., Fletcher, J., Waite, T.D., 2018. Integration of
523   photovoltaic energy supply with membrane capacitive deionization (MCDI) for salt
524   removal from brackish waters. Water Res. https://doi.org/10.1016/j.watres.2018.09.056.

525   Valdés, C.F., Betancur, Y., López, D., Gómez, C.A., Chejne, F., 2018. Effects of pyrolysis
526   atmosphere on the porous structure and reactivity of chars from middle and high rank
527   coals. Ing. e Investig. https://doi.org/10.15446/ing.investig.v38n1.64516.

528   Volpe, R., Menendez, J.M.B., Reina, T.R., Messineo, A., Millan, M., 2017. Evolution of chars
529   during slow pyrolysis of citrus waste. Fuel Process. Technol. 158, 255–263.
530   https://doi.org/10.1016/J.FUPROC.2017.01.015.

531   Volpe, R., Messineo, A., Millan, M., Volpe, M., Kandiyoti, R., 2015. Assessment of olive

532　　　wastes as energy source: Pyrolysis, torrefaction and the key role of H loss in thermal
533　　　breakdown. Energy. https://doi.org/10.1016/j.energy.2015.01.011.

534　Wang, X., Bai, S., Jin, Q., Li, S., Li, Yukun, Li, Yan, Tan, H., 2018. Soot formation during
535　　　biomass pyrolysis: Effects of temperature, water-leaching, and gas-phase residence time.
536　　　J. Anal. Appl. Pyrolysis. https://doi.org/10.1016/j.jaap.2018.07.015.

537　Wang, Y., Chung, S.H., 2019. Soot formation in laminar counterflow flames. Prog. Energy
538　　　Combust. Sci. https://doi.org/10.1016/j.pecs.2019.05.003.

539　Welgemoed, T.J., Schutte, C.F., 2005. Capacitive Deionization Technology^{TM}: An alternative
540　　　desalination solution. Desalination. https://doi.org/10.1016/j.desal.2005.02.054.

541　Yu, J., Lucas, J.A., Wall, T.F., 2007. Formation of the structure of chars during devolatilization
542　　　of pulverized coal and its thermoproperties: A review. Prog. Energy Combust. Sci.
543　　　https://doi.org/10.1016/j.pecs.2006.07.003.

544　Zabaniotou, A., Stavropoulos, G., Skoulou, V., 2008. Activated carbon from olive kernels in a
545　　　two-stage process: Industrial improvement. Bioresour. Technol. 99, 320–326.
546　　　https://doi.org/10.1016/J.BIORTECH.2006.12.020.

547　Zarzo, D., Prats, D., 2018. Desalination and energy consumption. What can we expect in the
548　　　near future? Desalination. https://doi.org/10.1016/j.desal.2017.10.046.

549　Zhang, D., Shi, L., Fang, J., Dai, K., 2007. Influence of diameter of carbon nanotubes mounted
550　　　in flow-through capacitors on removal of NaCl from salt water. J. Mater. Sci.
551　　　https://doi.org/10.1007/s10853-006-1293-z.

552　Zhang, T., Walawender, W.P., Fan, L.T., Fan, M., Daugaard, D., Brown, R.C., 2004.
553　　　Preparation of activated carbon from forest and agricultural residues through CO2
554　　　activation. Chem. Eng. J. 105, 53–59. https://doi.org/10.1016/J.CEJ.2004.06.011.

555　Zhang, Y., Chen, L., Mao, S., Sun, Z., Song, Y., Zhao, R., 2019. Fabrication of porous graphene
556　　　electrodes via CO2 activation for the enhancement of capacitive deionization. J. Colloid
557　　　Interface Sci. 536, 252–260. https://doi.org/10.1016/J.JCIS.2018.10.063.

558

559